Institut für Numerische Simulation

Rheinische Friedrich-Wilhelms-Universität Bonn

M. Griebel, J. Hamaekers

Molecular dynamics simulations of boron-nitride nanotubes embedded in amorphous Si-B-N

Molecular dynamics simulations of boron-nitride nanotubes embedded in amorphous Si-B-N

Michael Griebel, Jan Hamaekers [*]

Department of Numerical Simulation,
Division of Numerical Simulation in the Natural and Engineering Sciences,
University of Bonn, Wegelerstraße 6, D-53115 Bonn, Germany.

Abstract

In this article, we examine the elastic properties of boron-nitride nanotubes, which are embedded in amorphous silicon-boron-nitride ceramics. We employ molecular dynamics simulations using the Parrinello-Rahman approach. To this end, all systems are modeled with a reactive many-body bond order potential due to Tersoff, which is able to describe covalent bonding accurately. We apply external stress and derive stress-strain curves for various tensile and compressive load cases at given temperature and pressure. In addition to Young moduli and Possion ratios, we compare radial distribution functions, average coordination numbers, ring statistics and self-diffusion coefficients to characterize the short-range, medium-range and long-range order of Si_3BN_5, $Si_3B_2N_6$ and $Si_3B_3N_7$ matrices, respectively. Here, our results show that $Si_3B_3N_7$ exhibits the highest Young modulus and the largest elastic range. Then, we study the properties of a ceramics composite material made from $Si_3B_3N_7$ matrix and BN nanotubes. We calculate stress-strain curves for the composite to predict the rates of reinforcement of the matrix due to the BN nanotubes. Here, also the influence of the nanotube/matrix-ratio on the elastic modulus of the composite is examined. Finally, we compare the Young moduli derived from our numerical simulations to predictions given by both, a simple macroscopic rule-of-mixtures, which depends on the volume fraction only, and an extended rule-of-mixtures, which also takes the geometry of the BN nanotube into account. Our numerical results show that the extended rule-of-mixtures predicts the Young modulus of the composite with a relative error of 5% or less.

Key words: molecular dynamics simulations, boron-nitride nanotubes, Si-B-N ceramics, composites, elastic moduli
PACS: 02.70.Ns, 62.20.Dc, 62.25.+g, 81.05.Je, 83.10.Rs.

[*] Corresponding author. Tel.: +49 228 733173; fax: +49 228 737527.
Email address: hamaekers@ins.uni-bonn.de (Jan Hamaekers).

1 Introduction

Nanotubes [1] have attracted a lot of attention in the last decade due to their unusual structural properties. Besides the now well-known tubes made from carbon, there exist tubes made from other materials. In particular, boron-nitride (BN) nanotubes [2,3], and different types of $B_x C_y N_z$ [4,5] nanotubes were first predicted on the basis of computer simulations. Meanwhile, single and multi-wall formed BN nanotubes can be produced with diameters comparable to that of carbon nanotubes [6–8]. Several types of $B_x C_y N_z$ tubes have also been synthesized [9] and transformed to pure BN nanotubes [10]. Recently, ab-initio molecular dynamics simulations have been performed to simulate the microscopic growth mechanism for BN nanotubes [11] and the phonons of BN nanotubes [12]. Experimental studies [13] and semi-empirical calculations [5] of their mechanical properties show that BN nanotubes display a high Young modulus, which is at least comparable to that of carbon nanotubes. However, the electrical properties of BN nanotubes are very different from those of carbon nanotubes. While carbon nanotubes show a metallic, semiconductor or insulator characteristic depending on chirality and diameter, theoretical studies suggest that BN nanotubes exhibit an energy gap of about 4–5 eV independent of chirality, diameter or number of walls [3]. Thus, BN nanotubes possess the property of an insulator for low electric fields. Altogether, BN tubes are one of the strongest insulating nanofibers and may find important uses in ceramics and composites.

On the other hand, there exits a large variety of ceramics and amorphous materials. An interesting class is based on polycrystalline or amorphous siliconnitride which additionally contains boron or carbon. Some structural characterization of such systems has recently been achieved experimentally, see [14–16]. Such ceramics have various industrial applications [17,18] because of their unusual thermal and mechanical properties [19].

Therefore, it can be expected that a Si-B-N matrix with embedded BN nanotubes results in a promising new material with interesting properties. To our knowledge composites of Si-B-N ceramics and BN nanotubes have neither been theoretically studied nor been synthesized so far. To this end, computational methods can be used to access and thus to predict, to describe and to explain the mechanical and the thermal properties of such future materials [20]. Computer simulations allow detailed studies on the influence of different parameters on associated material properties, like the volume fraction and the geometric distribution of the nanotubes within the composite. In particular, first-principle techniques and empirical potential methods have been successfully applied to study several small nanoscaled systems. For large systems with thousands of atoms and more, classical molecular dynamics simulations must be used due to complexity reasons.

In this work, we first derive stress-strain curves of amorphous Si_3BN_5, $Si_3B_2N_6$ and $Si_3B_3N_7$ at various temperatures for normal pressure by means of classical molecular dynamics simulations in the framework of the NPT ensemble [21,22]. To model amorphous Si-B-N, we use the Tersoff bond order potential [23,24], which is able to describe covalent bonding in an accurate way. We apply an external stress tensor within the equations of motion of the Parrinello-Rahman-Nosé Lagrangian [21,22,25] to accomplish various tensile and compressive load cases. Furthermore, we characterize these systems by analyzing their short-range, medium-range and long-range order. For a better understanding of the medium-range order properties, we study the shortest-path rings in the amorphous matrix. To this end, we have to find all shortest-path rings within an interconnection network. Here, we improved the algorithm of Franzblau [26] with respect to the scalability of the storage and the computational effort for large sparse graphs. Our results show that amorphous $Si_3B_3N_7$ exhibits the highest Young modulus and the largest elastic range.

We then study the mechanical properties of $Si_3B_3N_7$ ceramics with embedded BN nanotubes. Here we are interested in the reinforcement of the amorphous matrix. To this end, we derive stress-strain curves for the composites at various temperatures for different nanotube/matrix ratios. We obtain reinforcement rates between 1% and 37% depending on the composition of the system and the considered temperature. In our equilibrated composite systems we find that between 6% and 13% of the atoms of the BN nanotubes are bonded to an atom of the $Si_3B_3N_7$ matrix.

Finally, we compare the results of our numerical simulations on the mechanical properties of the composites with two macroscopic rule-of-mixtures, which are commonly used to predict the Young modulus of composites. Here, the simple rule-of-mixtures depends on the Young modulus of the nanotube, the Young modulus of the matrix and the volume fraction of the nanotube. The relative error of this simple rule can be reduced by using an extended rule-of-mixtures due to Liu and Chen [27,28], which also takes the geometry of the nanotube, i.e. length and diameter, into account. This extended rule-of-mixtures then results in a relative error which is less than 5%.

The remainder of this paper is organized as follows: In section 2 we discuss the computational methods which we used in our studies. Here, in section 2.1, the details of the molecular dynamics approach in the framework of the NPT ensemble are given. In section 2.2 we discuss the potential model which we employ to represent systems composed of silicon, boron and nitrogen. We present the computational method used to derive stress-strain curves in section 2.3. The techniques to characterize the short-range, medium-range and long-range order are given in section 2.4 and 2.5. In section 3 we describe the setup of our numerical experiments. Their results are discussed in section 4. Finally we give some concluding remarks in section 5.

2 Computational methods

2.1 Molecular dynamics simulations

The Hamiltonian for a molecular system with N particles, constant volume and constant energy is given by

$$\mathcal{H} = \frac{1}{2} \sum_{i=1}^{N} \frac{\vec{p}_{\vec{x}_i}^T \vec{p}_{\vec{x}_i}}{m_i} + V(\vec{x}_1, \ldots, \vec{x}_N) \tag{1}$$

with cartesian coordinates $\vec{x}_i$, moments $\vec{p}_{\vec{x}_i}$, masses m_i and a conservative potential V. This corresponds to the so-called NVE ensemble. To obtain an isothermal-isobaric ensemble, or NPT ensemble, which allows to control pressure and temperature, we introduce additional degrees of freedom. To this end, we define a time-dependent matrix $\hat{h} = [\vec{a}_1, \vec{a}_2, \vec{a}_3]$ which consists of the basis vectors of the simulation cell and re-scale the coordinates by $\hat{\vec{s}}_i = \hat{h}^{-1} \vec{x}_i$. Furthermore, we re-scale the time t by $\bar{t} = \int_0^t \gamma(\tau) d\tau$ and thus obtain the velocities in the form $\dot{\vec{x}}_i(\bar{t}) = \gamma \hat{h} \dot{\hat{\vec{s}}}_i(t)$. This way, there are the nine degrees of freedom of the cell matrix $\hat{h}$ to control the pressure and one degree of freedom related to the scaling of the velocities γ to control the temperature. We define the fictitious potentials $P_{\text{ext}} \det \hat{h}$ and $N_f k_B T \ln \gamma$ with help of the external pressure P_{ext} and the target temperature T, the system's number of degrees of freedom N_f and Boltzmann's constant k_B. Now a so-called Parrinello-Rahman-Nosé Lagrangian can be postulated and an extended Hamiltonian

$$\begin{aligned}
\mathcal{H} = &\frac{1}{2} \sum_{i=1}^{N} \frac{\vec{p}_{\vec{s}_i}^T G \vec{p}_{\vec{s}_i}}{m_i} + \frac{1}{2} \frac{\text{tr}(p_h^T p_h)}{M_P} + \frac{1}{2} \frac{p_\eta^2}{M_T} \\
&+ V(h, h\vec{s}_1, \ldots, h\vec{s}_N) + P_{\text{ext}} \det h + N_f k_B T \eta
\end{aligned} \tag{2}$$

can be derived with dynamical variables $\vec{s}_i(t) := \hat{\vec{s}}_i(\bar{t})$, $h(t) := \hat{h}(\bar{t})$, $G := h^T h$, and $\eta(t) := \ln \gamma(\bar{t})$; for details see [20–22]. Here, M_P is a fictitious mass or inertia parameter to control the time-scale of motion of the cell h, and M_T is an analogous parameter with respect to the temperature. The related equations of motion read as

$$\dot{\vec{s}}_i = \frac{\vec{p}_{\vec{s}_i}}{m_i}, \quad \dot{h} = \frac{p_h}{M_P}, \quad \dot{\eta} = \frac{p_\eta}{M_T}, \tag{3}$$

$$\dot{\vec{p}}_{\vec{s}_i} = -h^{-1} \nabla_{\vec{x}_i} V - G^{-1} \dot{G} p_{\vec{s}_i} - \frac{p_\eta}{M_T} p_{\vec{s}_i}, \tag{4}$$

$$\dot{p}_h = (\Pi_{\text{int}} - \text{diag}(P_{\text{ext}})) h^{-T} \det h - \frac{p_\eta}{M_T} p_h, \tag{5}$$

$$\dot{p}_\eta = \sum_{i=1}^{N} \frac{\vec{p}_{\vec{s}_i}^T G \vec{p}_{\vec{s}_i}}{m_i} + \frac{\text{tr}(p_h^T p_h)}{M_P} - N_f k_B T, \tag{6}$$

4

with the internal stress tensor

$$\Pi_{\text{int}} = \frac{1}{\det h} \left(\sum_{i=1}^{N} m_i h \vec{s}_i \vec{s}_i^T h^T - \frac{d}{d\,h} V \right) h^T \,. \tag{7}$$

Note that if periodic boundary conditions are used, the potential V depends explicitly on the matrix h, since atoms in the unit cell interact not only with other atoms in the same unit cell but also with their translated images. These interactions must be correctly included in the terms $\frac{d}{d\,h} V$ and $\nabla_{\vec{x}_i} V$ within equation (4) and (7); for details see also [25].

Note that one third of the trace of the internal stress tensor equals the instantaneous internal pressure $P_{\text{int}} = \frac{1}{3} \text{tr}(\Pi_{\text{int}})$. Furthermore, the instantaneous temperature

$$T_{\text{instan}} = \frac{2 E_{\text{kin}}}{N_f k_B}$$

can be determined from the kinetic energy

$$E_{\text{kin}} = \frac{1}{2} \sum_{i=1}^{N} \frac{\vec{p}_{s_i}^T G \vec{p}_{s_i}}{m_i}$$

as usual; the thermodynamic temperature is the time-average of T_{instan}.

For the numerical solution of the system (3)–(6) of ordinary differential equations we have to employ a time-integration scheme. We use the "predictor-corrector" scheme based on Beeman's approach [29] with the modifications due to Refson [30]. This way, also the problem of the dependence of the forces on the velocities in the equations of motion (3)–(6) is circumvented. Furthermore, the expensive evaluation of the coordinate-dependent terms of the force calculation has to be performed just once. The evaluation of the velocity-dependent terms, which is relatively cheap, has in practice to be done about three times per time step.

Note finally that the physical energy $E_{\text{kin}} + V$ contained in the Hamiltonian (2) of an NPT ensemble is not conserved. This is in contrast to the Hamiltonian (1) of an NVE ensemble. But the Hamiltonian (2), i.e. the sum of the physical energy, the fictitious energy of the barostat and the fictitious energy of the thermostat, remains constant over time.

2.2 Potential for silicon, boron and nitrogen

There are different empirical potential models available for covalent Si-B-N systems, like the bond order potential of Tersoff [23] or the potential model of Marian and Gastreich [31,32]. In this work, we follow the approach of

Matsunaga and Iwamoto [24]. We choose the Tersoff potential and assume furthermore that the interactions between Si-B, B-B, and N-N are purely repulsive. This representation is free of effective atomic charges and includes short-ranged two- and three-body atom interactions. Moreover, the model allows the breaking and formation of bonds. The details of this potential and the parameters which we used to model Si-B-N systems are given in detail in [23,24]. Note that all interatomic terms are restricted by cut-off parameters. Thus the well-known linked cell technique can be used for an efficient implementation [33]. A straightforward domain decomposition approach then allows for a parallel implementation which results in a parallel complexity of the order $\mathcal{O}(N/P)$ [34,20]. Here, N denotes the number of particles and P the number of processors. This allows to treat systems with large numbers of particles in reasonable time.

2.3 Stress-strain relationship

The stress-strain relationship provides the overall mechanical response of a material which is subjected to mechanical loading. To account for tensile and compressive load, we use an additional external stress tensor Π_{ext} within the equations of motion (5)

$$\dot{p}_h = \left(\Pi_{\text{int}} - \text{diag}\left(P_{\text{ext}} \right) + \Pi_{\text{ext}} \right) h^{-T} \det h - \frac{p_\eta}{M_T} p_h \,. \qquad (8)$$

We first equilibrate the system with zero external stress and constrain the system to obtain a symmetric [1] equilibrated cell matrix h_{equi}. We then increase or decrease one of the six independent components of the symmetric external stress tensor over a period of time and measure the induced stress $\pi := -\Pi_{\text{int}}$ and the induced strain ε. Note that thus the linear strain tensor ε is equal to the symmetric part $\frac{1}{2}\left(e^T + e \right)$ of the displacement matrix $e = hh_{\text{equi}}^{-1} - 1$. This way, we generate a stress-strain curve for a tensile or compressive load at given temperature and pressure [25].

To determine elastic constants we assume that *Hooke's law* [35], which implies a linear stress-strain relationship, is fulfilled for small values of strain. Then, the slope of the stress-strain curve under uniaxial tension is equal to the so-called Young modulus E. Moreover, the ratio of transverse contraction strain to longitudinal extension strain in the direction of the stretching force is known as the Poisson ratio ν. Now, to compute the elastic constants E and ν of a system, we simulate this system under uniaxial tensile load and obtain a discrete stress-strain curve and a discrete transverse strain to longitudinal

---

[1] Note that the symmetry constraint reduces the number of degrees of freedom of h from 9 to 6.
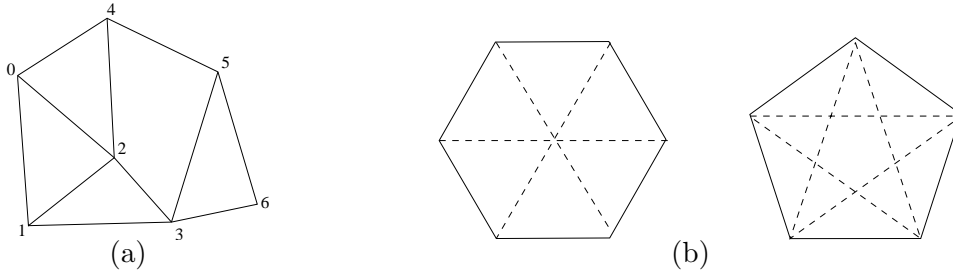
Fig. 1. (a) A graph with 7 vertices. The shortest-path rings of this graph are $021, 024, 01354, 123, 2354$ and 365. (b) Pairs of antipodes of rings with lengths $k = 6$ and $k = 7$. The pairs of antipodes are connected with dashed lines.

strain curve. Then, due to the assumption of Hooke's law, the approximative values of E and ν can be easily computed by least squares linear regression [36].

2.4 Shortest-path rings

One way to characterize the medium-range order of amorphous structures is to analyze the rings of the interconnection network. The computation of all rings up to a given maximal length k is essentially a graph theoretical problem [37]. Here, atoms are regarded as vertices $v \in V$ and bonds [2] as edges $e \in E$ in an abstract graph $G = (V, E)$. An approved method to derive meaningful information is to take only so-called shortest-path rings into account [38,26]. The shortest-path criterion is fulfilled, if a ring contains a shortest path for each pair of vertices within the ring. This way, only rings which have no shortcuts are counted; see also Figure 1(a). Franzblau has given an efficient algorithm to calculate all shortest-path rings up to a maximal length k [26]. We improved his method with respect to the scalability of the storage and computational cost in the case of networks with a small maximal coordination number n like amorphous Si-B-N ceramics.

The original algorithm creates the full distance matrix of the given undirected graph G. For this purpose, a minimal spanning tree is generated to each vertex $v \in V$ using breadth-first search. Then, a backtracking algorithm is performed for each $v \in V$ to find all shortest-path rings. Here, paths are successively excluded for which the following shortest-path ring criterion applies: A ring R of the length k is a shortest-path ring if the distance criterion $\text{dist}_R(u, v) = \text{dist}_G(u, v)$ is fulfilled for every pair of antipodes u, v; see also Figure 1(b). Here dist_R and dist_G denote the distance in a ring R and the graph G, respectively. Note that the distance matrix is used to evaluate the distance criterion efficiently. Furthermore, to reduce the number of rings, which grows

---

[2] The practical determination of bonds via distances between atoms will be discussed in section 4.2.

exponentially with $\frac{k}{2}$, an unimodal labeling according the distance to v is used. If all shortest-path rings involving v are found, the vertex v and its adjacent edges are deleted from the graph to avoid duplicate counting of shortest-path rings. Then, a new starting vertex is chosen and the procedure is repeated until all vertices are excluded from the graph. Due to the creation of the full distance matrix, the storage and computational cost of this approach grows quadratically in the number $N = |V|$ of vertices in the graph.

To reduce this complexity we developed a new algorithm in which the full distance matrix is not set up. Instead we exploit the sparsity of the interconnection networks related to amorphous systems. To this end, we use a labeling for all vertices and store for each vertex the indices of its neighbors. Then, we calculate for a starting vertex v the local subgraph which is related to the vertices with a distance less or equal $\frac{k}{2}$ only. The components of this subgraph are stored in a list ordered by the distance to the starting vertex v.[3] This way, we are able to search efficiently in the interconnection network. Furthermore, for amorphous systems we can assume that the number of vertices, which are linked by a path of length less than k, grows cubically with k only. Then, to find all shortest-path rings of length k, our algorithm has a storage complexity of the order $\mathcal{O}(Nk^3)$ and a computational complexity of the order $\mathcal{O}(Nn^{\frac{k}{2}} \log k)$, where n denotes the maximal coordination number. This way, we avoid the complexity of the order $\mathcal{O}(N^2)$ of the original algorithm. This is a significant improvement for large sparse graphs and small values of k which allows to treat substantially larger amorphous systems.

2.5 Further structural analysis

The short-range order of amorphous structures can be characterized in terms of the radial distribution or pair correlation functions. First, we define $\mathcal{T} := \{\text{Si}, \text{B}, \text{N}\}$ as the set of the atomic types of the observed system. Then the partial pair correlation function $g_{(\alpha,\beta)}(r)$ gives the probability to find an atomic pair of type $\alpha \in \mathcal{T}$ and $\beta \in \mathcal{T}$ with distance r [39]. It can be approximately evaluated from a histogram of pair distances accumulated over a simulation run with m time steps as follows: If $N_{(\alpha,\beta)}^{\text{bin}}([r, r+\Delta r))$ denotes the number of pairs of type (α, β) within the interval $[r, r+\Delta r)$, then $g_{(\alpha,\beta)}$ can be written as

$$g_{(\alpha,\beta)}([r, r+\Delta r)) \cong \frac{V}{N_\alpha N_\beta} \frac{N_{(\alpha,\beta)}^{\text{bin}}([r, r+\Delta r))}{\frac{4\pi}{3}\left((r+\Delta r)^3 - r^3\right)} \frac{1}{m} , \qquad (9)$$

where V denotes the volume of the system, N_α denotes the number of atoms of type $\alpha \in \mathcal{T}$, and m denotes the number of considered time steps. The

---

[3] If two vertices have the same distance from v, they are ordered according to their global label number.

computation of the histogram can easily be implemented within a linked cell approach [20]. Furthermore, the histogram can be used to calculate the average coordination number

$$n_{(\alpha,\beta)}(R) = \frac{1}{N_\alpha} \int_0^R N_{(\alpha,\beta)}^{\text{bin}}(r')\, dr',$$

(10)

which gives the average number of atomic species β in a sphere of radius R centered at atoms of type α. Note that in contrast to the partial pair correlation function $g_{(\alpha,\beta)}$, the average coordination number $n_{(\alpha,\beta)}$ is not symmetric in (α,β).

Long-range order properties like diffusion can be characterized by analyzing the mean square displacements. For a simulation with a time step size Δt, the mean square displacement for $t = \mu \Delta t$ of an atom-type $\alpha \in \mathcal{T}$ with N_α atoms can be approximately expressed as

$$\text{msd}_\alpha(t) \cong \frac{1}{N_\alpha m} \sum_{i \in \mathcal{T}_\alpha} \sum_{j=0}^{m-1} \| \vec{x}_i(t_{j+\mu}) - \vec{x}_i(t_j) \|^2\,, \quad t_\nu = \nu \Delta t\,.$$

(11)

Here, $\mathcal{T}_\alpha$ denotes the set of indices $i \in \{1,\dots,N\}$ for which the associated particle is of type α. Finally, to obtain the self-diffusion coefficient D_α of species $\alpha \in \mathcal{T}$, we have the expression

$$D_\alpha = \lim_{t \to \infty} \frac{1}{6t} \text{msd}_\alpha(t)$$

which is based on the Einstein relation [39]. Thus, for large t, we obtain a good approximation to the diffusion coefficients.

3 Numerical experiments

We have incorporated the computational methods described in section 2 into our existing molecular dynamics software package TREMOLO which is a load-balanced distributed memory parallel code [20]. For further details see the web page `http://www.ins.uni-bonn.de/info/md`. All numerical experiments were performed on our PC cluster Parnass2 [40]. This parallel computing system consists of 128 Intel Pentium II 400 MHz processors connected by a 1.28 GBit/s switched Myrinet. To integrate the equations of motion (3)–(6), we used the method discussed in section 2.1 with a time step size of 0.1 fs. The fictitious mass M_T for the thermostat was set to $10.0\,\text{uÅ}^2$ and the fictitious mass M_P for the barostat was set to $10.0\,\text{u}$. Furthermore, we applied periodic boundary conditions.
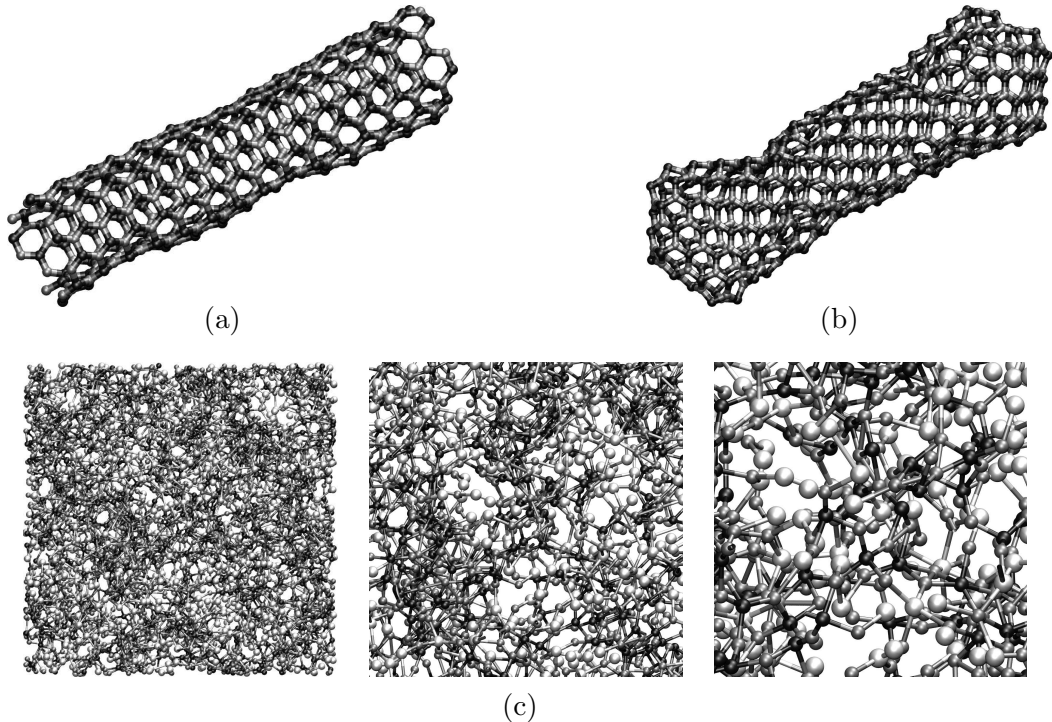
Fig. 2. Equilibrated systems: (a) A continuous (12,0) BN nanotube (system I). (b) A capped (12,0) BN nanotube. (c) Three views into a $Si_3B_3N_7$ matrix composed of 4254 atoms.

3.1 Equilibrated systems

We first equilibrated a $(12,0)$ BN nanotube using a NPT-ensemble under normal pressure at a temperature of $300\,K$ over $40\,ps$. This nanotube consists of 360 atoms and is approximately $36\,\text{Å}$ long; see also Figure 2(a). Here, we used an unit cell of appropriate size and applied periodic boundary conditions to simulate an infinitely elongated nanotube. In the following we denote this system as *system I*. To permit the unit cell to alter in longitudinal direction only, we applied appropriate constraints to the associated Hamiltonian (2).

Furthermore, we equilibrated amorphous systems for Si_3BN_5, $Si_3B_2N_6$, and $Si_3B_3N_7$ with a total number of atoms of 3831, 4070, and 4254, respectively. To this end, the atoms were randomly placed into a cubic simulation cell and we performed an NPT-ensemble at $3500\,K$ with a pressure of $40\,GPa$ over 10.0 ps to eliminate the effect of the initial atomic configuration. Then, we decreased the temperature linearly to $1500\,K$ over $40\,ps$, kept the temperature constant for $20\,ps$, linearly decreased it again to $300\,K$ over $20\,ps$, and finally equilibrated at $300\,K$ for $20\,ps$. Here, we started the equilibration process with a diagonal cell matrix and allowed axial variation only. We obtained a density of approximately $2.6\,g/cm^3$ for the different equilibrated matrices. Note that in the case of the $Si_3B_3N_7$ matrix our calculated density is just slightly lower

Table 1
Equilibrated composite systems. Here, Ω_f denotes the approximate volume fraction of the BN nanotube, N_{mat} denotes the number of atoms of the matrix, h_{tt} denotes the approximate length of the transversal axes of the matrix, h_{ll} denotes the approximate length of the longitudinal axis of the matrix, N_{tub} denotes the number of atoms of the BN nanotube and L_{tub} denotes the approximate length of the BN nanotube.

System	Ω_f [%]	N_{mat}	h_{tt} [Å]	h_{ll} [Å]	N_{tub}	L_{tub} [Å]
II	7.8	4254	36	36	360	36
III	4.5	8508	36	72	456	41
IV	2.3	17016	36	143	456	41
V	3.3	17016	36	143	648	60
VI	4.5	17016	36	143	888	82
VII	0.8	68064	71	143	648	60
VIII	1.1	68064	71	143	888	82
IX	1.2	136128	71	285	1848	170

than the predicted density of approximately $2.8\,\mathrm{g/cm^3}$ given in reference [41].

To obtain an equilibrated system for the continuous BN nanotube embedded in the $Si_3B_3N_7$ matrix, we followed the approach of Brown [42]: We created a cylindrical cavity in the already relaxed $Si_3B_3N_7$ matrix of appropriate size by using a soft repulsive potential [43] within a local minimization process. We then placed the continuous BN nanotube in the cylindrical cavity and performed an isothermal-isobaric molecular dynamics simulation under normal pressure at a temperature of $300\,\mathrm{K}$ for $40\,\mathrm{ps}$ to equilibrate the composite; see also Figure 3(a). We denote this system as *system II*. In an analog way, we generated seven more composites consisting of a $Si_3B_3N_7$ matrix and a (12,0) capped BN nanotube. We denote these systems of different size and nanotube/matrix-ratio as *system III–IX*; for more details see Table 1 and Figure 3. Note that we finally employed a further equilibration process over $40\,\mathrm{ps}$ to obtain equilibrated systems under normal pressure at a given target temperature.

3.2 Tensile and compressive load conditions

We used the equilibrated reference systems to perform tensile and compressive tests. To this end, we applied an external stress tensor in the framework of the NPT-ensemble as described in section 2.3. In particular, we employed a stress rate of $0.01\,\mathrm{GPa/ps}$ to increase or decrease external stress for the longitudinal axial component in our tensile and compressive load experiments, respectively. The results of these numerical simulations are presented and discussed in the following section 4.
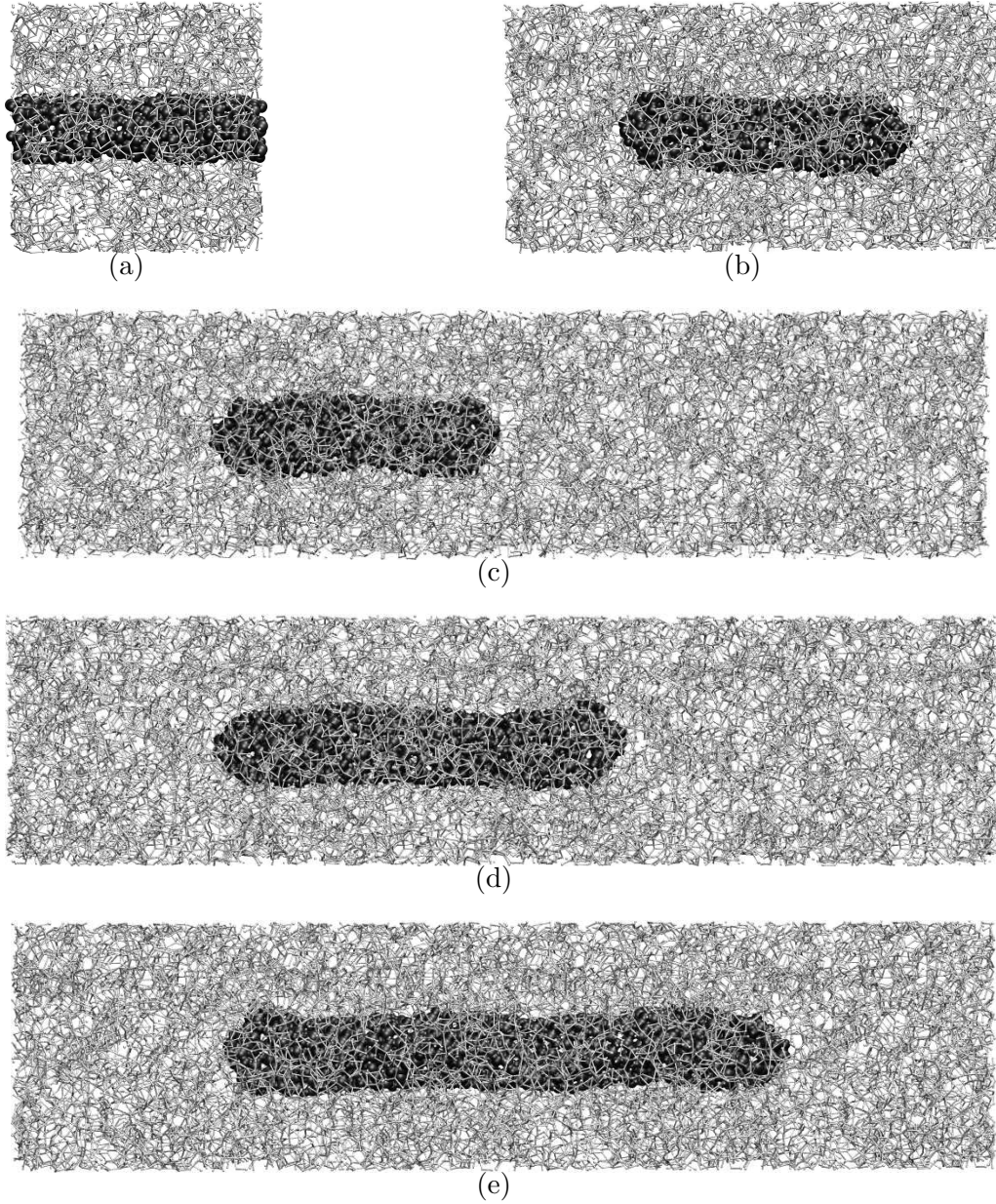
Fig. 3. The unit cells of the equilibrated systems II–VI: (a) System II. (b) System III. (c) System IV. (d) System V. (e) System VI.

4   Results and discussion

4.1   BN *nanotubes*

For the infinite BN nanotube (system I) our tensile tests show that the maximal load, which can be reached before fracture occurs, decreases with increasing temperature; see Figure 4(a) and 4(b). The computed Young moduli are in the range of 650 GPa to 700 GPa for temperatures between 300 K and 1200 K.
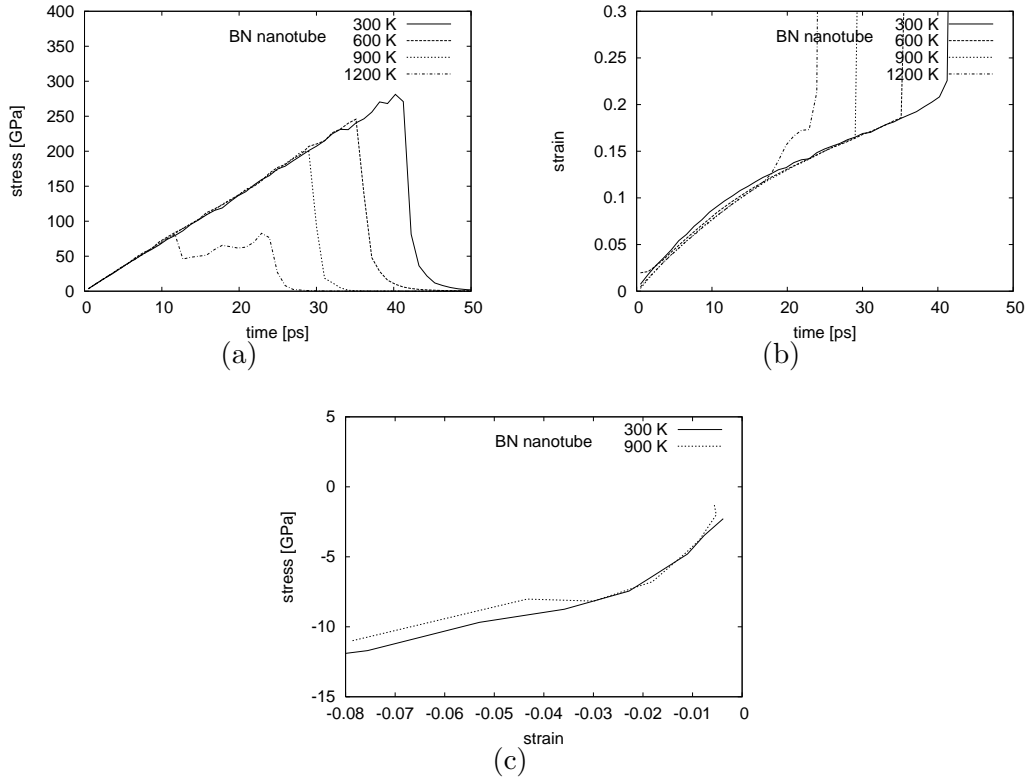
(a)

(b)

(c)

Fig. 4. (a) Stress-time curve for the continuous BN nanotube (system I) under tensile load. (b) Strain-time curve for system I under tensile load. (c) Stress-strain curve for system I under compressive load.

Also, the Young modulus decreases with the increase of the temperature; for detailed results see Table 3. For the compressive test case, the computed stress-strain curve is depicted in Figure 4(c). The change in the slope indicates that buckling occurs at a strain rate of approximately -0.03. Some intermediate snapshots of the BN nanotube from the simulated tensile and compressive load cases are given in Figure 5.

4.2 Si-B-N matrices

We now study the structural and mechanical properties of different Si-B-N matrices. Here, we focus on Si_3BN_5, $Si_3B_2N_7$ and $Si_3B_3N_7$.

First we deal with the short-range order of these materials via partial pair correlation functions $g_{(\alpha,\beta)}$. Here, the pairs (Si, Si), (Si, N) and (B, N) are modeled by a repulsive and an attractive interaction term whereas the pairs (Si, B), (B, B) and (N, N) are modeled by a repulsive interaction term only. Altogether, our computations clearly show the amorphous structure of these Si-B-N matrices. Detailed results for 300 K are given in Figure 6.

13

(a)   (b)   (c)

(d)   (e)   (f)
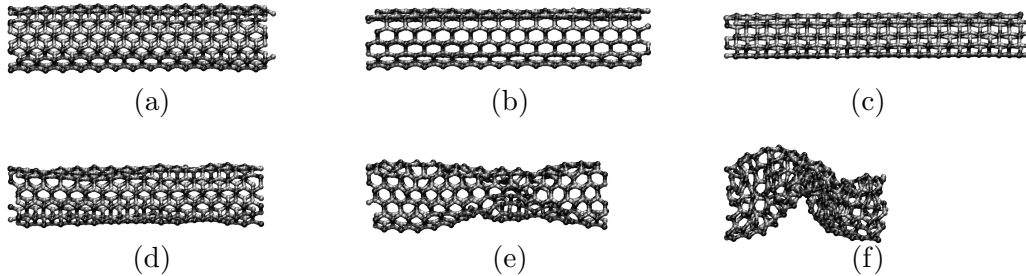
Fig. 5. Snapshots of simulations of a continuous BN nanotube (*system I*) under tensile and compressive load conditions: (a) Uniaxial load of 36.8 GPa with a strain of 0.05. (b) Uniaxial load of 102.5 GPa with a strain of 0.11. (c) Uniaxial load of 289.8 GPa with a strain of 0.21. (d) Uniaxial load of -4.7 GPa with a strain of -0.01. (e) Uniaxial load of -10.2 GPa with a strain of -0.05. (f) Uniaxial load of -21.5 GPa with a strain of -0.37.

For a pair $(\alpha, \beta) \in \mathcal{B} := \{(\mathrm{Si}, \mathrm{Si}), (\mathrm{Si}, \mathrm{N}), (\mathrm{B}, \mathrm{N})\}$, we denote the first local minimum in the associated pair correlation function $g_{(\alpha,\beta)}$ as $R_{(\alpha,\beta)}$. We then characterize a pair of atoms (i, j) of type $(\alpha, \beta) \in \mathcal{B}$ as *bonded*, if their distance r_{ij} is less than $R_{(\alpha,\beta)}$. Note that the distances $R_{(\alpha,\beta)}$ are approximately equal to the corresponding cut-off radii of the Tersoff potential model [24]. With the help of $R_{(\alpha,\beta)}$ and the partial pair correlation functions $g_{(\alpha,\beta)}$, we then calculate the average coordination numbers $n_{(\alpha,\beta)}$ according to equation (10). The resulting values are depicted for varying temperature in Figure 7. We observed that the computed average coordination numbers are approximately constant up to a temperature of 1200 K. With an increasing amount of boron the average coordination numbers $n_{(\mathrm{Si},\mathrm{Si})}$ and $n_{(\mathrm{N},\mathrm{B})}$ increase whereas the average coordination numbers $n_{(\mathrm{Si},\mathrm{N})}$ and $n_{(\mathrm{N},\mathrm{Si})}$ decrease. Note that our calculated average coordination numbers underestimate experimental results given in reference [15]. For the case of the $\mathrm{Si_3B_3N_7}$ matrix, values of $n_{(\mathrm{B},\mathrm{N})} = 2.8$–$2.9$, $n_{(\mathrm{N},\mathrm{B})} = 1.2$–$1.4$, $n_{(\mathrm{Si},\mathrm{N})} = 3.4$–$3.7$ and $n_{(\mathrm{N},\mathrm{Si})} = 1.4$–$1.6$ have been obtained. This is possibly due to a slight difference in the set up used in the experiment and in our simulations.

We now characterize the medium-range order in $\mathrm{Si_3BN_5}$, $\mathrm{Si_3B_2N_6}$ and $\mathrm{Si_3B_3N_7}$ by analyzing the shortest-path rings of the connection networks. Our computations show that the fraction of the shortest-path rings with length $5 \leq k \leq 10$ is for 1500 K smaller than for the lower temperatures, whereas the fraction of shortest-path rings with length $k = 3$ is for 1500 K larger than for the lower temperatures; see Figure 8. This indicates that the amorphous Si-B-N matrices break down to components with only two or three atoms for a temperature of 1500 K. In addition, we found that the ratio of shortest-path rings with a length of $k \leq 5$ is increasing with the amount of boron, which suggests an strengthening effect on the amorphous network.

Then, we analyzed atomic transport properties of the equilibrated Si-B-N ma-
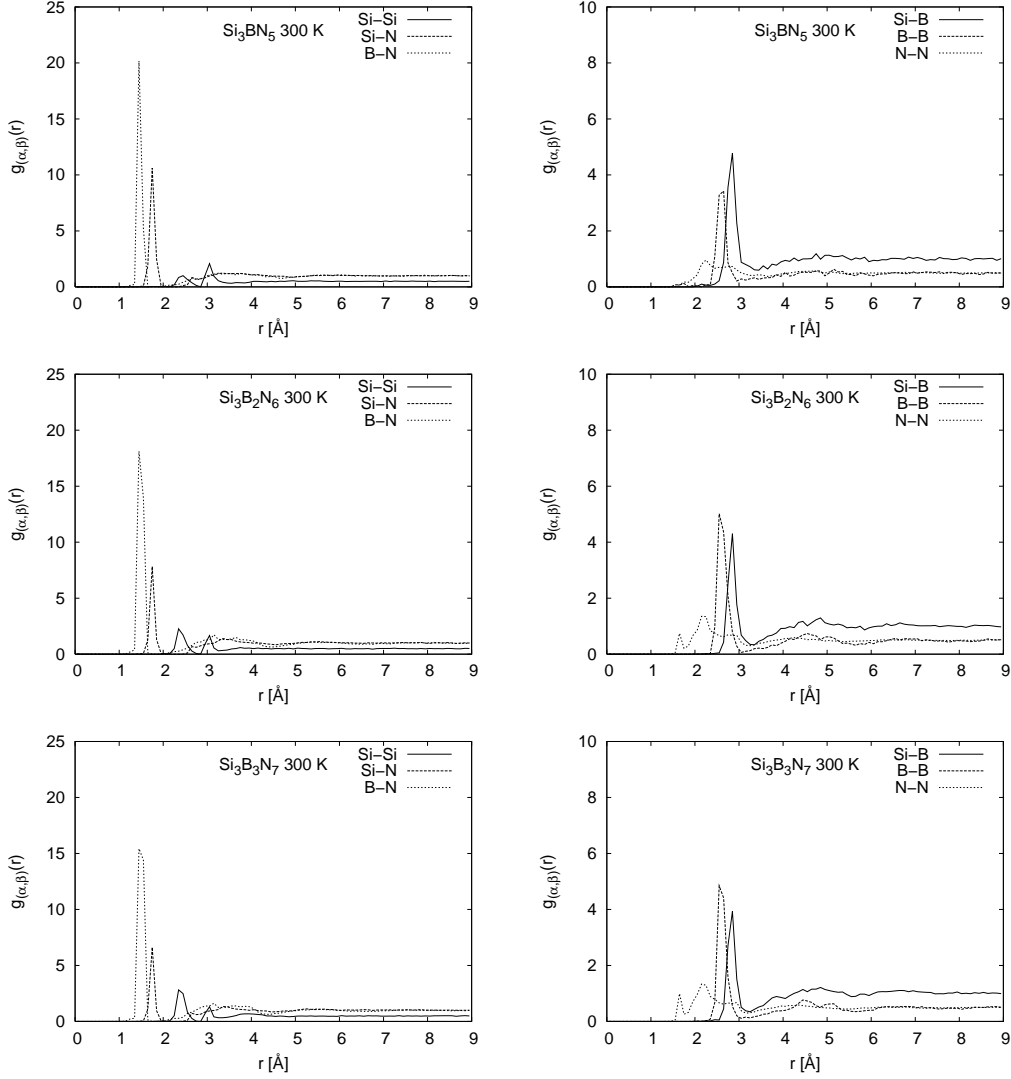
Fig. 6. Partial pair correlation functions for equilibrated Si_3BN_5, $Si_3B_2N_6$ and $Si_3B_3N_7$ at a temperature of 300 K under normal pressure.

trices, which are of long-range order. Here, the self-diffusion coefficients of the $Si_3B_3N_7$ and $Si_3B_2N_6$ matrices are much smaller than that of the Si_3BN_5 matrix; see Figure 9. Note that for high temperatures between 1200 K and 1500 K, the self-diffusion coefficients decrease with the increase of the amount of boron. This indicates that $Si_3B_3N_7$ exhibits the best thermal stability, which is in a good agreement with the results of the molecular dynamics simulations of Matsunaga and Iwamoto; for a further discussion see [24]. Note that our results for the average coordination numbers, the shortest-path rings and the self-diffusion coefficients suggest that there is a change of phase between 1200 K and 1500 K. In experimental studies of amorphous $Si_3B_3N_7$, a decomposition temperature of approximately 1950 K has been determined [15]. This difference is probably due to the Tersoff potential model and slight discrepancies in the set up of the experiment and our simulations.

15
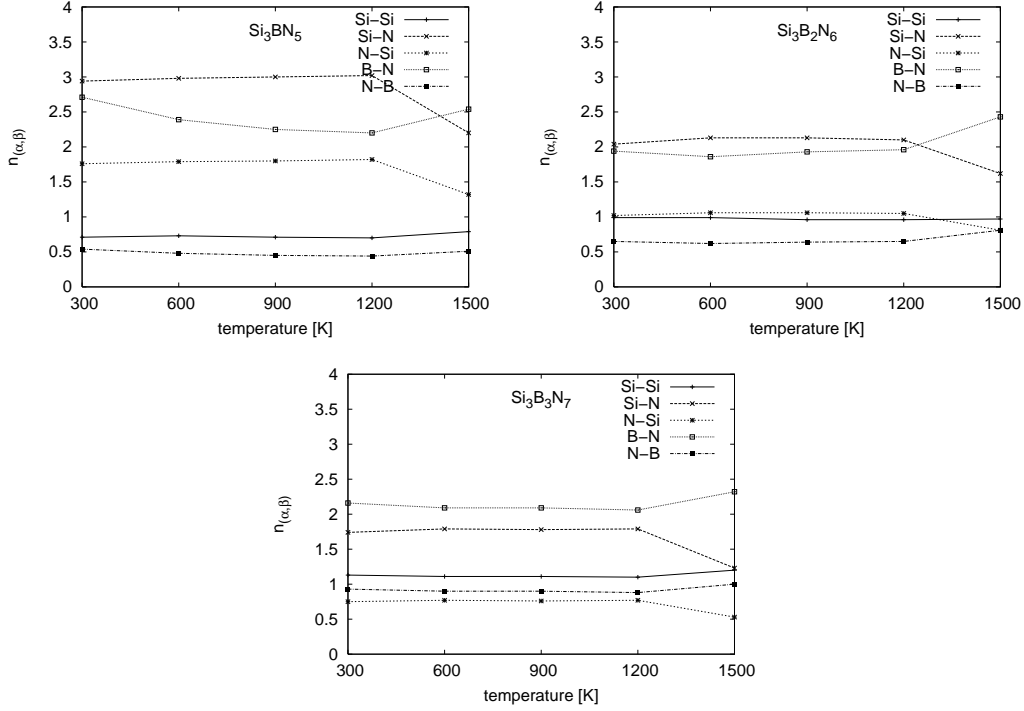
Fig. 7. Average coordination numbers for Si_3BN_5, $Si_3B_2N_6$ and $Si_3B_3N_7$ under normal pressure.

Finally, we studied the mechanical properties of the Si-B-N matrices. Here, the computed stress-strain curves for the tensile and compressive load cases show that the Young modulus and the elastic range increase with increasing amount of boron; see Figure 10. In particular, in correspondence with the suggested change of phase between 1200 K and 1500 K, the computed stress-strain curves indicate that the Young modulus and the elastic range is rapidly decreasing from temperature 1200 K to temperature 1500 K; see Figure 11. Moreover, our results of the tensile tests show that the average coordination numbers, especially $n_{(B,N)}$ and $n_{(N,B)}$, decrease with an increase of the external stress; see Figure 12. Also, the fraction of the shortest-path rings with length $5 \leq k \leq 12$ decreases with an increase of the external stress; compare Figure 13. Note that, in the case of $Si_3B_3N_7$, our computed Young moduli decrease from 132.1 GPa at 300 K to 129.5 GPa at 1200 K; see Table 3. This is slightly lower than the theoretical predictions of the Young modulus of $Si_3B_3N_7$ ($\approx$ 200 GPa) given in [41] and the experimental values for related Si-B-(C)-N ceramics ($\approx$ 200–350 GPa) given in [14]. Nevertheless, the experimental studies also showed a decrease of the Young modulus with an increase of the temperature [14].

Altogether, as already noted, our results suggest that the decomposition temperature increases with the amount of boron. Furthermore, our results on the mechanical properties of Si_3BN_5, $Si_3B_2N_6$ and $Si_3B_3N_7$, indicate that $Si_3B_3N_7$ exhibits the highest Young modulus and the largest elastic range. Therefore we focus in the following on composites of BN nanotubes and amorphous
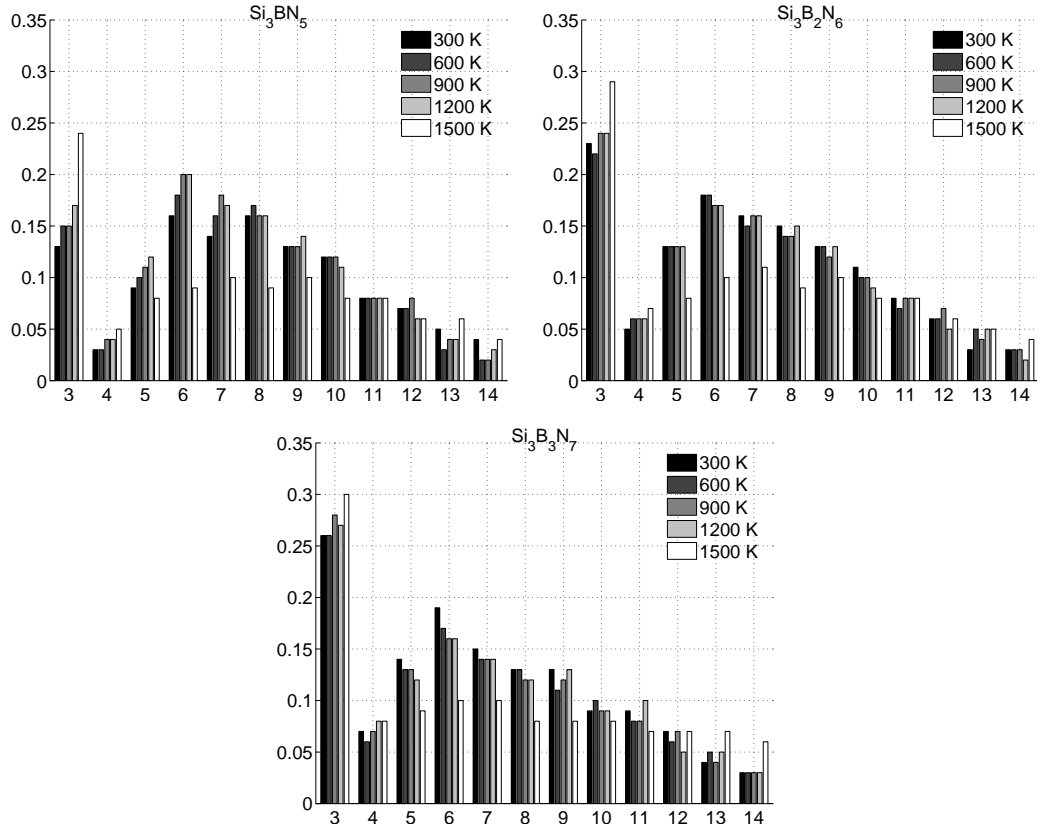
16

Fig. 8. Histograms of the distribution of the length of shortest-path rings of equilibrated amorphous Si_3BN_5, $Si_3B_2N_6$ and $Si_3B_3N_7$ at various temperatures under normal pressure.

$Si_3B_3N_7$. Here, due to the expected change of phase for temperatures above 1200 K, we consider only temperatures between 300 K and 1200 K.

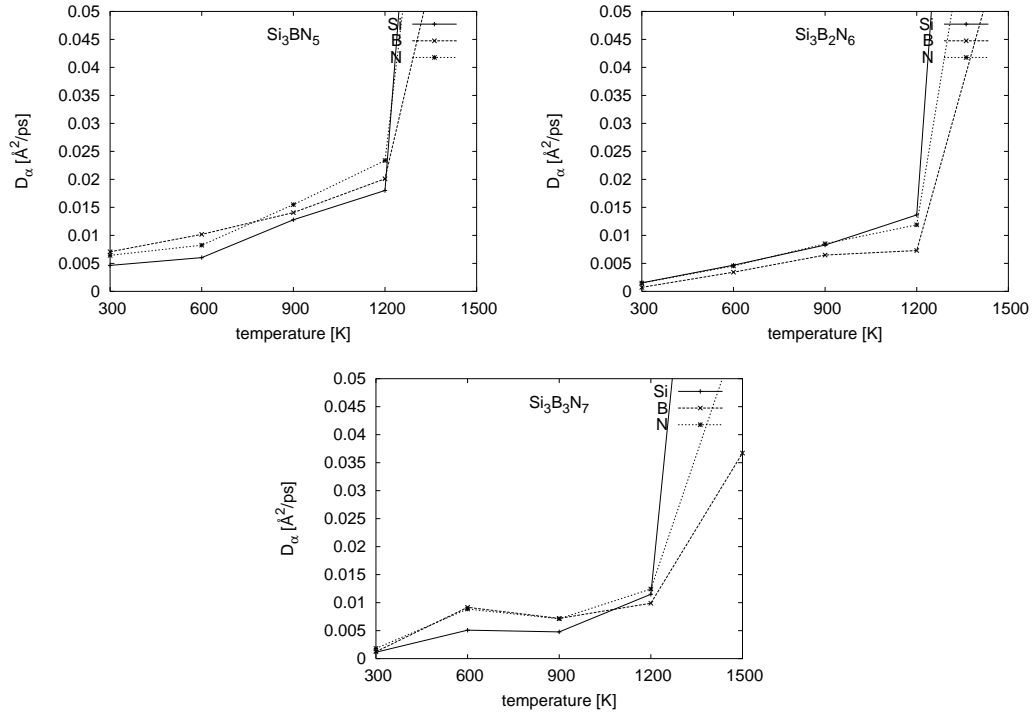Fig. 9. Self-diffusion coefficients of amorphous Si_3BN_5, $Si_3B_2N_6$ and $Si_3B_3N_7$ at different temperatures under normal pressure.
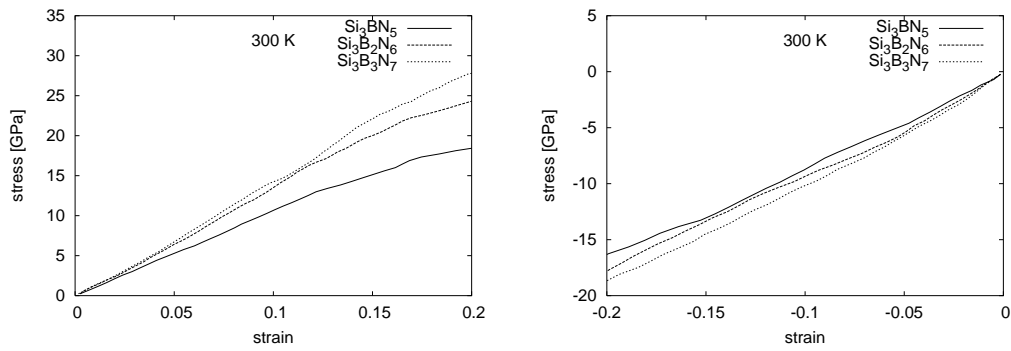
Fig. 10. Stress-strain curves of amorphous Si_3BN_5, $Si_3B_2N_6$ and $Si_3B_3N_7$ for the tensile load case at a temperature of $300\,K$.
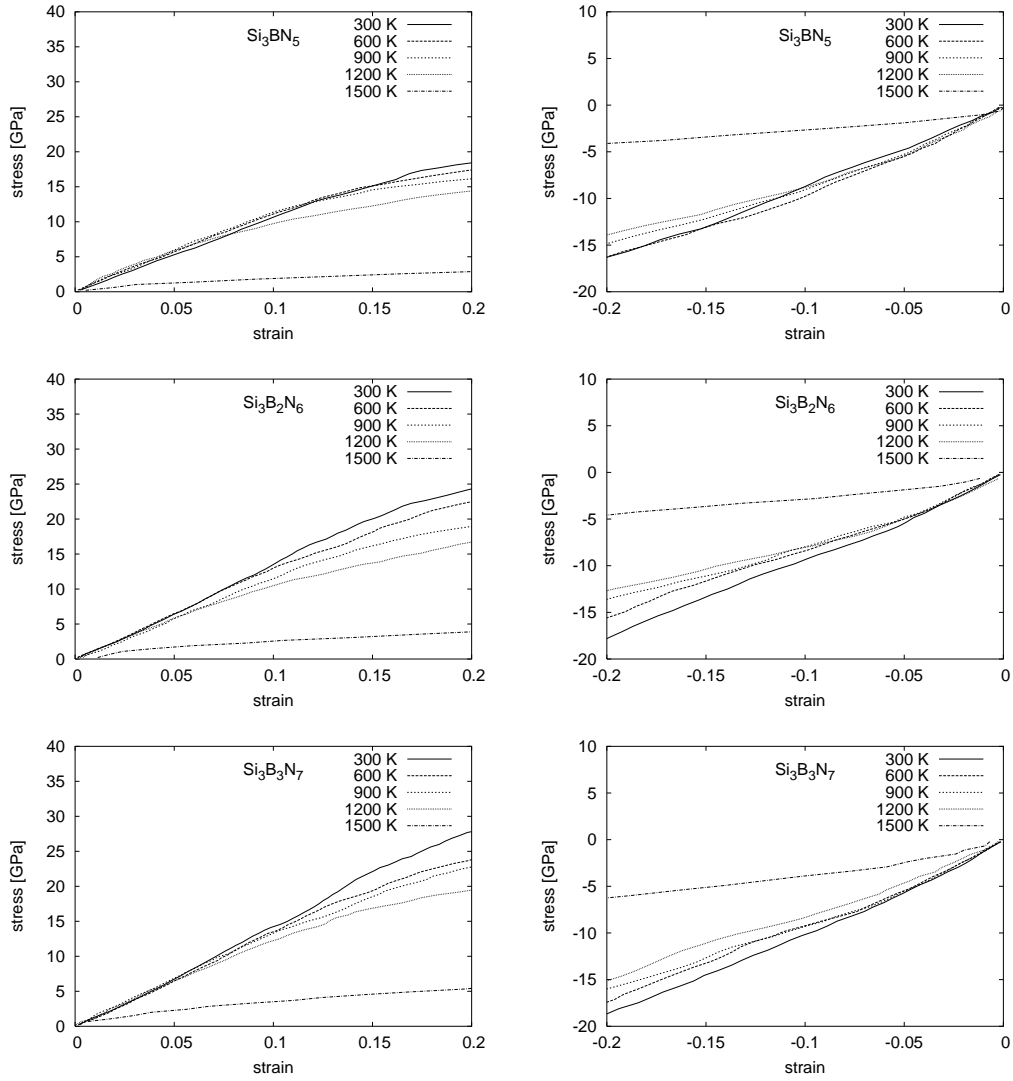
Fig. 11. Stress-strain curves of amorphous $Si_3B_3N_7$, $Si_3B_2N_6$ and Si_3BN_5 for the tensile and compressive load cases at various temperatures under normal pressure.
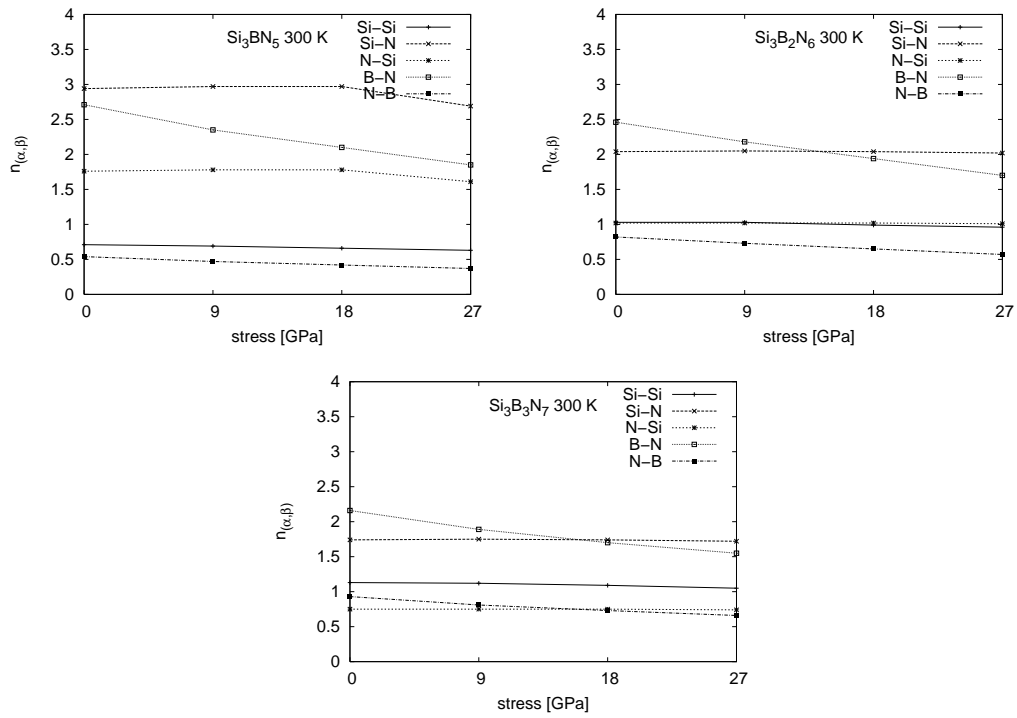
Fig. 12. Average coordination numbers for Si_3BN_5, $Si_3B_2N_6$, $Si_3B_3N_7$; during tensile load case at a temperature of $300\,K$.
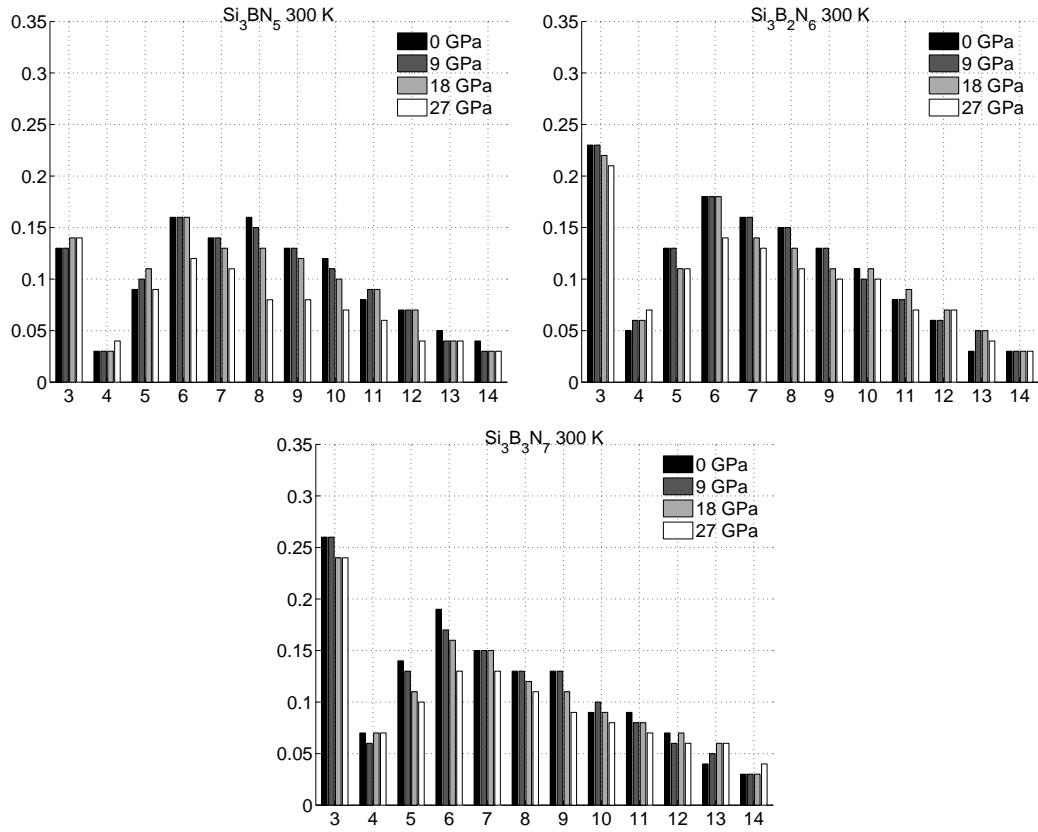
Fig. 13. Histograms of the distribution of the length of shortest-path rings of amorphous Si_3BN_5, $Si_3B_2N_6$ and $Si_3B_3N_7$; during tensile load case at a temperature of 300 K.
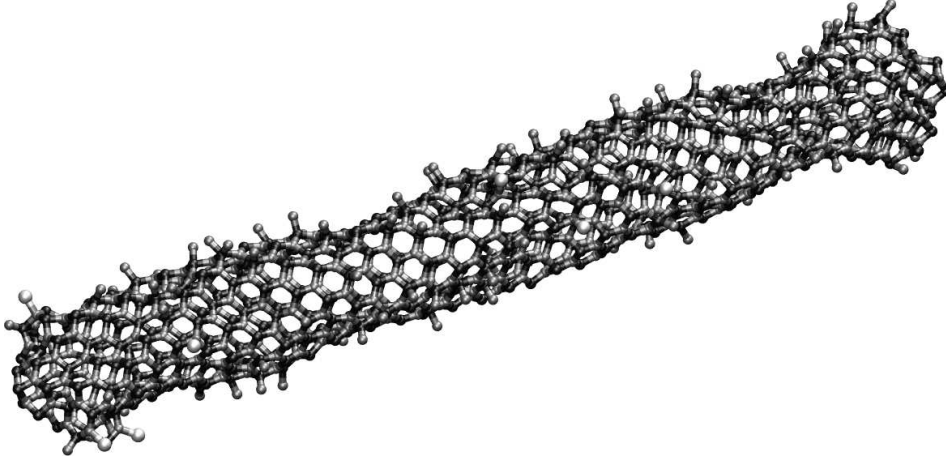
Fig. 14. Partial view of system VI. Here we only show the atoms of the BN nanotube and the atoms of the matrix which are bonded to the nanotube.
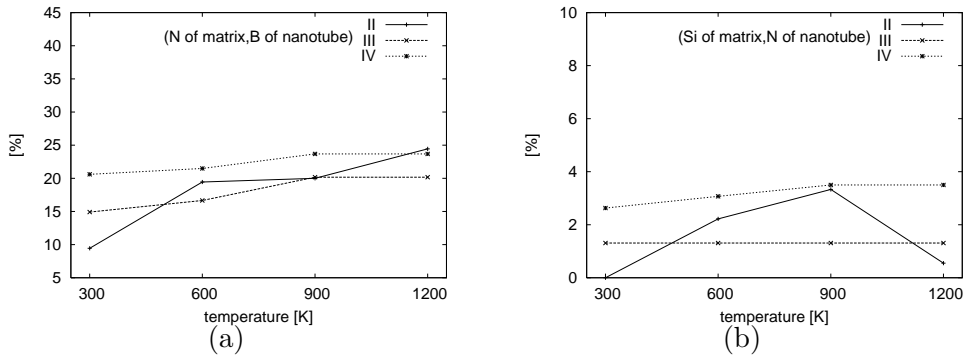

Fig. 15. (a) Percentage of the boron atoms of the nanotube which are bonded to a nitrogen atom of the matrix for systems II–IV. (b) Percentage of the nitrogen atoms of the nanotube which are bonded to a silicon atom of the matrix for systems II–IV.

4.3 BN *nanotube* / $Si_3B_3N_7$ *composites*

First we consider the interaction between a BN nanotube and a $Si_3B_3N_7$ in a composite; see also Figure 14. The equilibrated systems II–IX exhibit two types of interconnection bonds[4] between the nanotube and the matrix. Primarily, there are bonds between boron atoms of the nanotube and nitrogen atoms of the matrix. Here, the amount of boron atoms of the nanotube, which are bonded to a nitrogen atom of the matrix, is 15–25 % of the overall amount of boron atoms of the nanotube; see Figure 15(a) and Table 2(a). Then, there are bonds between nitrogen atoms of the nanotube and silicon atoms of the matrix. Here, the amount of bonded nitrogen atoms of the nanotube is less than 4 %; see Figure 15(b) and Table 2(b). Note that van der Waals interactions are

---

[4] As already noted we characterize a pair of atoms (i, j) of type $(\alpha, \beta) \in \{(Si, Si), (Si, N), (B, N)\}$ as bonded if their distance r_{ij} is less than $R_{(\alpha, \beta)}$.

Table 2
(a) Percentage of the boron atoms of the nanotube which are bonded to a nitrogen atom of the matrix for systems V–IX at a temperature of 300 K. (b) Percentage of the nitrogen atoms of the nanotube which are bonded to a silicon atom of the matrix for systems V–IX at a temperature of 300 K.

	System V	System VI	System VII	System VIII	System IX
(a)	20.3 %	21.2 %	14.4 %	15.1 %	13.6 %
(b)	2.5 %	1.6 %	1.0 %	3.1 %	2.4 %

Table 3
Young moduli E and Poisson ratios ν of BN nanotube $Si_3B_3N_7$ composites at various temperatures under normal pressure. Additionally, the Young moduli and Poisson ratios of the $Si_3B_3N_7$ matrix are given.

	$Si_3B_3N_7$		System I	System II		System III		System IV	
T [K]	E [GPa]	ν	E [GPa]	E [GPa]	ν	E [GPa]	ν	E [GPa]	ν
300	132.2	0.27	696.1	181.5	0.24	150.2	0.25	139.1	0.27
600	131.7	0.30	671.6	171.8	0.30	148.9	0.27	136.6	0.29
900	130.0	0.29	665.6	169.0	0.32	145.4	0.30	136.1	0.31
1200	129.5	0.32	657.8	164.2	0.30	145.1	0.32	135.7	0.36

not modeled within the Tersoff bond order potential we used.

To characterize the mechanical properties of composites of BN nanotubes and amorphous $Si_3B_3N_7$, we computed stress strain curves related to tensile load conditions for the $Si_3B_3N_7$ matrix and system I to system IV, respectively. The derived elastic constants are given in Table 3. Depending on the temperature, our results predict a reinforcement of 27% to 37% for the case of the composite with the (periodically) infinite BN nanotube (system II). Note that this constitutes an upper limit for all other systems with equal nanotube/matrix volume fraction. For system III we obtain a reinforcement of approximately 12–14 % and for system IV we observe a reinforcement of 4–5 %. Note that the volume fraction of the BN nanotube in system IV is about one half of the volume fraction in system III. For the systems V to IX with 300 K we obtain a Young modulus of 141.9 GPa, 148.7 GPa, 133.5 GPa, 134.9 GPa and 137.0 GPa, respectively. The corresponding rates of reinforcement are given in Figure 16. Note that we see here an almost linear dependency of the reinforcement rate on the volume fraction. This shows that, from a macroscopic point of view, it makes sense to use so-called *rule-of-mixtures* to quantitatively describe the reinforcement properties of our composites by a simple formula. This will be discussed in the following.

For a nanocomposite, a simple macroscopic rule-of-mixtures can be used to estimate the Young modulus. It depends on the volume fraction Ω_f of the nanotube. This rule reads as

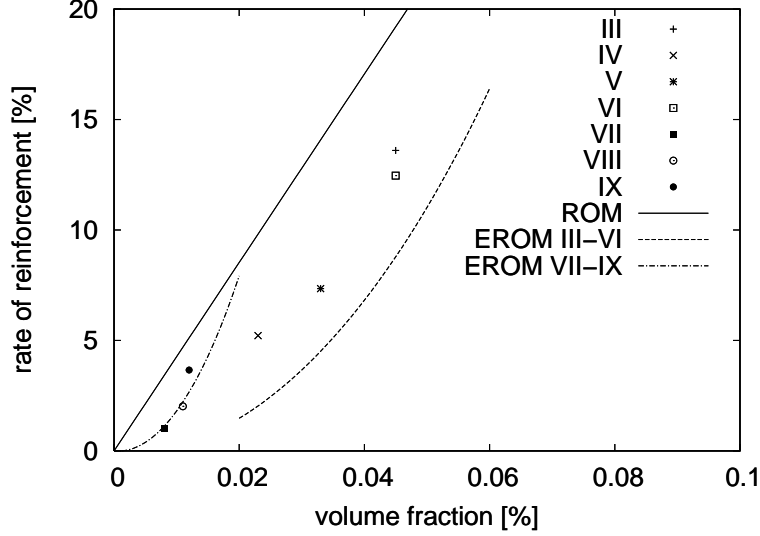$$E_c = \Omega_f E_f + (1 - \Omega_f)E_m , \qquad (12)$$

Fig. 16. Rates of reinforcement of the Young moduli of the systems III–IX with respect to the Young modulus of the $Si_3B_3N_7$ matrix. Additionally, we have depicted the prediction with the help of the rule-of-mixtures (ROM) given in (12) and the extended rule-of-mixtures (EROM) given in (13). Here, to derive the rate of reinforcement as a function of the volume fraction only, we set in (13) the area of the cross-section to two specific constants for systems III–VI and for systems VII–IX, respectively.

where E_c denotes the predicted Young modulus of the composite and E_f denotes the Young modulus of the matrix. Following Liu and Chen [27,28] a more elaborated macroscopic rule-of-mixtures, which takes also the geometry of the nanotube into account, can be used to estimate the Young modulus of the systems III–IX. This extended rule-of-mixtures can be written in the form

$$E_c^{\text{ex}} = \left(\frac{1}{E_m} \frac{(L - L_c)}{L} + \frac{1}{E_c} \frac{L_c}{L} \frac{A}{A_c} \right)^{-1} . \tag{13}$$

Here, E_c^{ex} denotes the predicted Young modulus of the composite, L_c denotes the length of the nanotube, L is the length of the system related to the longitudinal axis, R_{in} denotes the inner radius of the nanotube, A denotes the area of the cross-section and A_c is defined as $A_c = A - \pi R_{\text{in}}^2$, respectively, see also Figure 17. In Figure 16 we give the predicted rates of reinforcement in dependence of the volume fraction for systems III–VI and systems VII–IX, respectively.[5] Furthermore, the relative errors of the rule-of-mixtures (12) and

---

[5] Note that for given inner and outer radii R_{in} and R_{out} of the nanotube and given values E_m, E_f and A, the extended rule-of-mixtures (13) degenerates to a function of the volume fraction Ω_f only. For the graphs of (13) in Figure 16 we assume the same values for E_m, E_f, R_{in} and R_{out}. Furthermore we keep the area A of the cross-section fixed to $1273 \, \text{Å}^2$ for systems III–VI and we set A to $5034 \, \text{Å}^2$ for systems VII–IX.
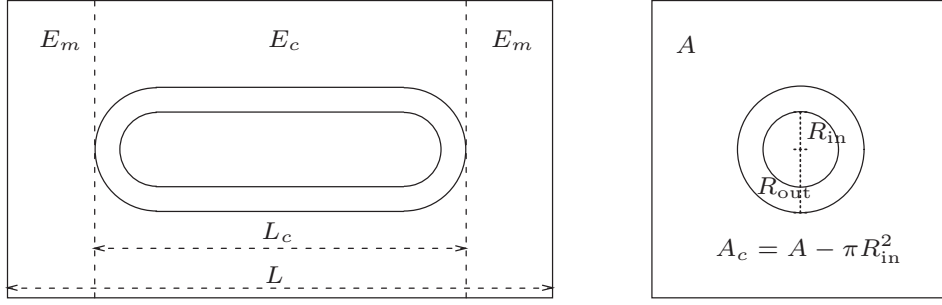
Fig. 17. Schematic diagram in respect to the extented rule-of-mixtures given in equation (13).

Table 4
The relative errors of the rule-of-mixtures (ROM) given in (12) and the extended rule-of-mixtures (EROM) given in (13) for systems II–IV.

T [K]	System II	System III		System IV	
	ROM	ROM	EROM	ROM	EROM
300	-0.0284	0.0501	-0.0411	0.0433	-0.0305
600	0.0091	0.0472	-0.0401	0.0538	-0.0175
900	0.0143	0.0604	-0.0288	0.0451	-0.0265
1200	0.0492	0.0635	-0.0293	0.0467	-0.0274

Table 5
The relative errors of the rule-of-mixtures (ROM) given in (12) and the extended rule-of-mixtures (EROM) given in (13) for systems V–IX.

T [K]	System V		System VI		System VII		System VIII		System IX	
	ROM	EROM	ROM	EROM	ROM	EROM	ROM	EROM	ROM	EROM
300	0.064	-0.026	0.060	-0.032	0.026	0.002	0.028	0.004	0.014	-0.010

(13) for the results of the numerical tensile experiments of systems II–IV are given in Table 4 and that of the systems V–IX can be seen in Table 5. The relative error with equation (12) and system II is less then 5 %. For system III and system IV we obtain values between 4.3 % and 6.4 % depending on the temperature. System V and system VI exhibit a relative error about 6 % and system VII to system IX exhibit an relative error of less than 3 %. In the case of system III to system IX the relative error is further reduced by the use of the extended rule-of-mixtures (13).

Altogether our results show that the simple rule-of-mixtures gives an upper limit for the Young modulus of the composite. The extended rule-of-mixtures is more accurate. Note finally that the simple rule-of-mixtures overestimates the Young modulus of the composite in many cases and the extended rule-of-mixtures underestimates the Young modulus of the composite in many cases.

5 Concluding remarks

In this article we studied composites made from Si-B-N matrices and BN nanotubes by means of molecular dynamics simulations. We employed the Parrinello-Rahman approach. Load was applied at different temperatures to derive stress-strain curves and to calculate elastic constants like the Young modulus and the Poisson ratio. We used the Tersoff potential to model BN nanotubes and amorphous Si_3BN_5, $Si_3B_2N_6$ and $Si_3B_3N_7$. We analyzed the short-range, medium-range and long-range order properties of these materials. Our simulations show that amorphous $Si_3B_3N_7$ possesses the highest Young modulus and the largest elastic range. Furthermore, we computed the mechanical properties of composites of BN nanotubes and $Si_3B_3N_7$ matrices. The calculated Young moduli were compared to the predictions from two different macroscopic rule-of-mixtures. The simple rule, which just takes the volume fraction of the nanotube into account, can be used for composites with the (periodically) infinitely long BN nanotube only. The extended rule, which also takes the geometry of the nanotube into account, can be applied for composites with fully embedded BN nanotubes. It predicts the Young modulus with a relative error of 5% or less. For the future a more refined rule-of-mixtures is needed, which additionally takes the density of cross-links at the matrix/nanotube interface into account [44].

Our simulation results show that BN nanotubes can be used to reinforce Si-B-N ceramics, at least theoretically. Now, experimental work is needed to practically synthesize this suggested composite material and to determine its characteristic properties.

6 Acknowledgments

References

[1] S. Iijima, Helical microtubules of graphitic carbon, Nature 354 (1991) 56–58.

[2] A. Rubio, J. L. Corkill, M. L. Cohen, Theory of graphitic boron nitride nanotubes, Phys. Rev. B 49 (1994) 5081–5048.

[3] X. Blase, A. Rubio, S. G. Louie, M. L. Cohen, Stability and band gap constancy of boron-nitride nanotubes, Europhys. Lett. 28 (1994) 335.

[4] Y. Miyamoto, A. Rubio, S. G. Louie, M. L. Cohen, Electronic properties of tubule forms of hexagonal BC_3, Phys. Rev. B 50 (1994) 18360–18366.

[5] E. Hernández, C. Goze, P. Bernier, A. Rubio, Elastic properties of C and $B_xC_yN_z$ composite nanotubes, Phys. Rev. Lett. 80 (20) (1998) 4502–4505.

[6] Y. Chen, J. F. Gerald, J. S. Williams, S. Bulcock, Synthesis of boron nitride nanotubes at low temperatures using reactive ball milling, Chem. Phys. Lett. 299 (1999) 260–264.

[7] O. R. Lourie, C. R. Jones, B. M. Bartlett, P. C. Gibbons, R. S. Ruoff, W. E. Buh, CVD growth of boron nitride nanotubes, Chem. Mater. 12 (2000) 1808–1810.

[8] M. Terauchi, M. Tanaka, K. Suzuki, A. Ogino, K. Kimura, Production of zigzag-type BN nanotubes and BN cones by thermal annealing, Chem. Phys. Lett. 324 (2000) 359–364.

[9] Z. Weng-Sieh, K. Cherrey, N. G. Chopra, X. Blase, Y. Miyamoto, A. Rubio, M. L. Cohen, S. G. Louie, A. Zettl, R. Gronsky, Synthesis of $B_xC_yN_z$ nanotubules, Phys. Rev. B 51 (1995) 11229–11232.

[10] W.-Q. Han, W. Mickelson, J. Cumings, A. Zettl, Transformation of $B_xC_yN_z$ nanotubes to pure BN nanotubes, Appl. Phys. Lett. 81 (6) (2002) 1110–1112.

[11] X. Blase, A. D. Vita, J.-C. Charlier, R. Car, Frustration effects and microscopic growth mechanisms for BN nanotubes, Phys. Rev. Lett. 80 (8) (1998) 1666–1669.

[12] L. Wirtz, A. Rubio, R. A. de la Concha, A. Loiseau, Ab-initio calculations of the lattice dynamics of boron nitride nanotubes, Phys. Rev. B 68 (2003) 045425.

[13] B. G. Demczyk, J. Cumings, A. Zettl, R. O. Ritchie, Structure of boron nitride nanotubules, Appl. Phys. Lett. 78 (18) (2001) 2772–2774.

[14] H.-P. Baldus, M. Jansen, High-performance ceramics – amorphous inorganic networks from molecular precursors, Angew. Chem. Int. Ed. Engl. 36 (1997) 328–343.

[15] R. M. Hagenmayer, U. Müller, C. J. Benmore, J. Neuefeind, M. Jansen, Structural studies on amorphous silicon boron nitride $Si_3B_3N_7$: Neutron contrast technique on nitrogen and high-energy X-ray diffraction, J. Mater. Chem. 9 (1999) 2865–2870.

[16] G. Jeschke, K. Kroschel, M. Jansen, A magnetic resonance study on the structure of amorphous networks in the Si-B-N(-C) system, J. Non-Cryst. Solids 260 (1999) 216–227.

[17] R. J. Brook, Materials science: Superhard ceramics, Nature 400 (1999) 312–315.

[18] F. Aldinger, Werkstoffe, die die Welt verändern – Hochleistungskeramiken machen den etablierten Materialien Konkurrenz, Phys. Bl. 55 (1999) 31–37.

[19] H.-P. Baldus, M. Jansen, D. Sporn, Ceramic fibers for matrix composites in high-temperature engine applications, Science 285 (1999) 699–703.

[20] M. Griebel, S. Knapek, G. Zumbusch, A. Caglar, Numerische Simulation in der Moleküldynamik. Numerik, Algorithmen, Parallelisierung, Anwendungen, Springer, Berlin, Heidelberg, 2003.

[21] M. Parrinello, R. Rahman, Crystal structure and pair potentials: A molecular-dynamics study, Phys. Rev. Lett. 45 (14) (1980) 1196–1199.

[22] S. Nosé, M. L. Klein, Constant pressure molecular dynamics for molecular systems, Molec. Phys. 50 (5) (1983) 1055–1076.

[23] J. Tersoff, Modeling solid-state chemistry: Interatomic potentials for multicomponent systems, Phys. Rev. B 39 (8) (1989) 5566–5568.

[24] K. Matsunaga, Y. Iwamoto, Molecular dynamics study of atomic structure and diffusion behavior in amorphus silicon nitride containing boron, J. Am. Ceram. Soc. 84 (10) (2001) 2213–2219.

[25] M. Griebel, J. Hamaekers, Molecular dynamics simulations of the elastic moduli of polymer-carbon nanotube composites, Computer Methods in Applied Mechanics and Engineering 193 (17–20) (2004) 1773–1788.

[26] D. S. Franzblau, Computation of ring statistics for network models of solids, Phys. Rev. B 44 (10) (1991) 4925–4930.

[27] Y. J. Liu, X. L. Chen, Evaluations of the effective material properties of carbon nanotube-based composites using a nanoscale representative volume element, Mechanics of Materials 35 (2003) 69–81.

[28] X. L. Chen, Y. J. Liu, Square representative volume elements for evaluating the effective material properties of carbon nanotube-based composites, Computational Materials Science 29 (2004) 1–11.

[29] D. Beeman, Some multistep methods for use in molecular dynamics calculations, J. Comp. Phys. 20 (1976) 130–139.

[30] K. Refson, Molecular dynamics simulation of solid n-butane, Physica B 131 (1985) 256–266.

[31] C. M. Marian, M. Gastreich, A systematic theoretical study of molecular Si/N, B/N, and Si/B/N(H) compounds and parameterisation of a force-field for molecules and solids, J. Mol. Struct. (TC) 506 (2000) 107–129.

[32] M. Gastreich, J. D. Gale, C. M. Marian, Charged-particle potential for boron nitrides, silicon nitrides, and borosilazane ceramics: Derivation of parameters and probing of capabilities, Phys. Rev. B 68 (2003) 094110.

[33] R. W. Hockney, J. W. Eastwood, Computer Simulation Using Particles, McGraw-Hill, New York, 1981.

[34] D. Beazley, P. Lomdahl, N. Gronbech-Jensen, R. Giles, P. Tamayo, Parallel algorithms for short-range molecular dynamics, in: D. Stauffer (Ed.), Annual Reviews of Computational Physics, Vol. III, World Scientific, 1995, p. 119.

[35] D. S. Chandrasekharaiah, L. Debnath, Continuum Mechanics, Academic Press, San Diego, 1994, Ch. 9.2.

[36] W. H. Press, S. A. Teukolsky, W. T. Vetterling, B. P. Flannery, Numerical Recipes - The Art of Scientific Computing, Cambridge University Press, Cambridge, 1992, Ch. 12.1.

[37] R. Diestel, Graph theory, Vol. 173 of Graduate Texts in Mathematics, Springer, 1991.

[38] C. S. Marians, L. W. Hobbs, Network properties of crystalline polymorphs of silica, J. Non-Cryst. Solids 124 (1990) 242–253.

[39] M. Allen, D. Tildesley, Computer simulation of liquids, Clarendon Press, Oxford, 1987.

[40] http://wissrech.ins.uni-bonn.de/research/projects/parnass2/index.html, parnass2 consists of 128 Intel Pentium II 400 MHz processors connected by a 1.28 GBit/s switched Myrinet.

[41] P. Kroll, R. Hoffmann, Silicon boron nitrides: Hypothetical polymorphs of $Si_3B_3N_7$, Angew. Chem. Int. Ed. 37 (18) (1998) 2527–2530.

[42] D. Brown, P. Mélé, S. Marceau, N. D. Albérola, A molecular dynamics study of a model nanoparticle embedded in a polymer matrix, Macromolecules 36 (2003) 1395–1406.

[43] D. Brown, The *gmq* user manual, version 3 (1999).

[44] S. J. V. Frankland, A. Caglar, D. W. Brenner, M. Griebel, Molecular simulation of the influence of chemical cross-links on the shear strength of carbon nanotube-polymer interfaces, J. Phys. Chem. B 106 (2002) 3046–3048.